

## Hyperion, IKONOS, ALI, and ETM+ sensors in the study of African rainforests

Prasad S. Thenkabail<sup>a,\*</sup>, Eden A. Enclona<sup>b,c</sup>, Mark S. Ashton<sup>b,c</sup>,  
Christopher Legg<sup>d</sup>, Minko Jean De Dieu<sup>e</sup>

<sup>a</sup>International Water Management Institute (IWMI), P.O. Box 2075, Street 127, Sunil Mawatha, Pelawatte, Battaramulla, Colombo, Sri Lanka

<sup>b</sup>Center for Earth Observation, Yale University, USA

<sup>c</sup>School of Forestry and Environmental Studies, Yale University, USA

<sup>d</sup>International Institute of Tropical Agriculture, Ibadan, Nigeria

<sup>e</sup>ONADEP, Cameroon

Received 3 March 2003; received in revised form 21 November 2003; accepted 25 November 2003

### Abstract

The goal of this research was to compare narrowband hyperspectral Hyperion data with broadband hyperspatial IKONOS data and advanced multispectral Advanced Land Imager (ALI) and Landsat-7 Enhanced Thematic Mapper Plus (ETM+) data through modeling and classifying complex rainforest vegetation. For this purpose, Hyperion, ALI, IKONOS, and ETM+ data were acquired for southern Cameroon, a region considered to be a representative area for tropical moist evergreen and semi-deciduous forests. Field data, collected in near-real time to coincide with satellite sensor overpass, were used to (1) quantify and model the biomass of tree, shrub, and weed species; and (2) characterize forest land use/land cover (LULC) classes.

The study established that even the most advanced broadband sensors (i.e., ETM+, IKONOS, and ALI) had serious limitations in modeling biomass and in classifying forest LULC classes. The broadband models explained only 13–60% of the variability in biomass across primary forests, secondary forests, and fallows. The overall accuracies were between 42% and 51% for classifying nine complex rainforest LULC classes using the broadband data of these sensors. Within individual vegetation types (e.g., primary or secondary forest), the overall accuracies increased slightly, but followed a similar trend. Among the broadband sensors, ALI sensor performed better than the IKONOS and ETM+ sensors.

When compared to the three broadband sensors, Hyperion narrowband data produced (1) models that explained 36–83% more of the variability in rainforest biomass, and (2) LULC classifications with 45–52% higher overall accuracies. Twenty-three Hyperion narrowbands that were most sensitive in modeling forest biomass and in classifying forest LULC classes were identified and discussed.

© 2004 Elsevier Inc. All rights reserved.

**Keywords:** African rainforests; Biomass models; Carbon flux; Hyperion; IKONOS; ALI; ETM+; Most sensitive Hyperion bands; Accuracy assessments; Broadbands; Narrowbands; Hyperion vegetation indices

### 1. Introduction

We are at the beginning of an era of spaceborne hyperspectral and hyperspatial sensors with the recent availability of data from the Hyperion, IKONOS, Advanced Land Imager (ALI), and Landsat-7 Enhanced Thematic Mapper Plus (ETM+). Given that older generation sensors have many known limitations with respect to their suitability

for studying complex biophysical characteristics (De Jong et al., 2000; Salas et al., 2002; Sampson et al., 2001; Steininger, 2000), the need to evaluate the new generation of sensors is of critical importance. This is particularly true in the rainforests, where vegetation complexity, spatial variability, diversity, and dynamics are at their highest levels. Accurate quantification of forest biophysical and biochemical attributes is essential for biodiversity assessment, land cover characterization, biomass modeling and carbon flux estimation (Blackburn & Milton, 1995).

High spectral resolution facilitates the identification of features while high spatial resolution permits accurate location of features (Gross & Scott, 1998). Advanced

\* Corresponding author. Tel.: +94-1-867404, +94-1-869080/1, +94-1-872178, +94-1-872181; fax: +94-1-866854.

E-mail address: [p.thenkabail@cgiar.org](mailto:p.thenkabail@cgiar.org) (P.S. Thenkabail).

multispectral sensors also allow significantly improved signal to noise ratios (Lévesque & King, 2003). The Hyperion, ALI, ETM+, and IKONOS sensors have a wide range of pixel sizes, radiometric resolutions, and spectral domains (Table 1) and are well suited for studying the complex biophysical and land use/land cover (LULC) characteristics of the rainforests.

The recent operational status of the Hyperion, the first spaceborne hyperspectral sensor launched onboard the Earth Observing-1 (EO-1) platform by the National Aeronautics and Space Administration's (NASA) New Millennium Program (NMP), requires new approaches to extracting information about vegetation from a large data volumes. The Hyperion gathers near-continuous data in 220 discrete narrowbands along the 400–2500-nm spectral range at a 30-m spatial resolution and in 16-bits (Table 1). The volume of data collected from Hyperion is about 75 times greater than that for an equivalent area from six non-thermal Landsat ETM+ bands. It is imperative that new methods

and techniques be developed to handle these high-dimensional data sets. At the same time, it will be important to optimize future hyperspectral sensors by identifying and dropping redundant bands. This will require determining the most sensitive wavebands for a given application. Optimizing hyperspectral sensors will help reduce the volume and dimensionality of the data sets, and make it feasible to apply traditional classification methods on the few selected bands that capture most of the pertinent information. In contrast to the Hyperion sensor, the IKONOS, ETM+, and ALI sensors gather data over broader spectral bandwidths (Table 1). A number of recent studies have indicated the advantages of using discrete narrowband data from specific portions of the spectrum, rather than broadband data, to obtain the most sensitive quantitative or qualitative information on crop or vegetation characteristics (e.g., Blackburn, 1999; Carter, 1998; Elvidge & Chen, 1995; Thenkabail et al., 2000b). However, none of these studies used spaceborne hyperspectral data or data for rainforests.

Table 1  
Image acquisition date and spatial, spectral, and radiometric sensor characteristics of data used in this study

Sensor	Acquisition date (and season) <sup>a</sup>	Spatial resolution (m)	Spectral bands	Radiometric resolution	Band range (nm)	Band centers (nm)	Band widths (nm)
<i>(A) Hyper-spectral sensor</i>							
(1) Hyperion	March 21, 2002 (end dry)	30	196 <sup>b</sup> , 157 <sup>c</sup>	16-bit	196–10-nm bands from 427–2395 nm	VNIR band centers start at 427.55 to 925.85 nm; SWIR band centers start at 932.72 to 2395.53 nm	10 nm wide (approx.) for all 196 bands
<i>(B) Hyper-spatial sensor</i>							
(1) IKONOS	February 5, 2002 (dry)	4	4	11-bit	445–516	480	71
					506–595	550	89
					632–698	664	66
	March 18, 2001 (end dry)				757–853	805	96
<i>(C) Multi-spectral sensors</i>							
(1) ALI multispectral	March 21, 2002 (end dry)	30	9	16-bit	433–453	443	20
					450–515	483	65
					425–605	565	180
					633–690	660	57
					775–805	790	30
					845–890	868	45
					1200–1300	1250	100
					1550–1750	1560	200
					2080–2350	2225	270
(2) Landsat-7 ETM+	March 18, 2001 (end dry)	30	6	8-bit	450–515	482	65
					525–605	565	80
					630–690	660	60
					750–900	825	150
					1550–1750	1650	200
					2090–2350	2220	260

<sup>a</sup> Local acquisition times: 10:45 AM (IKONOS), 10:15 AM (ETM+), 10:16 AM (Hyperion and ALI).

<sup>b</sup> Only 196 unique, calibrated bands. These are: (i) bands 8 (427.55 nm) to 57 (925.85 nm) in the visible and near-infrared; and (ii) bands 79 (932.72 nm) to band 224 (2395.53 nm) in the short wave infrared.

<sup>c</sup> There was significant noise in the data over the 1206–1437, 1790–1992, and 2365–2396 nm spectral ranges. When the Hyperion bands in this region were dropped, 157 useful bands remained.

A new era in hyperspatial data has been ushered in with the launch of the 1–4-m resolution IKONOS sensor (Table 1). The 11-bit IKONOS data is available for only four broad spectral bands. The ETM+ and ALI sensors also provide data for only in a few broadbands (Table 1), but have additional wavebands in the mid-infrared (MIR) that are known to be valuable in modeling forest structure, species composition, and moisture regime (Boyd & Duane, 2001). The 1.3–2.5- $\mu\text{m}$  band spans the short wave infrared (SWIR) portion of the spectrum but is widely referred to as a MIR band in the literature (e.g., Kumar et al., in press), a convention we adopt below.

The availability of data from the four new generation sensors (Hyperion, ALI, ETM+, and IKONOS) provides a

unique opportunity to characterize and model the biotic characteristics of rainforests and to establish a comparative study of the sensors. The main goal of this research was to determine the relative strengths and limitations of the narrowband hyperspectral Hyperion, broadband hyperspatial IKONOS, and multispectral broadband ALI and ETM+ sensor data for characterizing forest biomass and LULC. Specific objectives included:

- (1) determining the most sensitive Hyperion wavebands for characterizing rainforest vegetation; and
- (2) comparison of the ability of the four sensors to classify vegetation and predict biomass across and within rainforest vegetation and LULC classes.

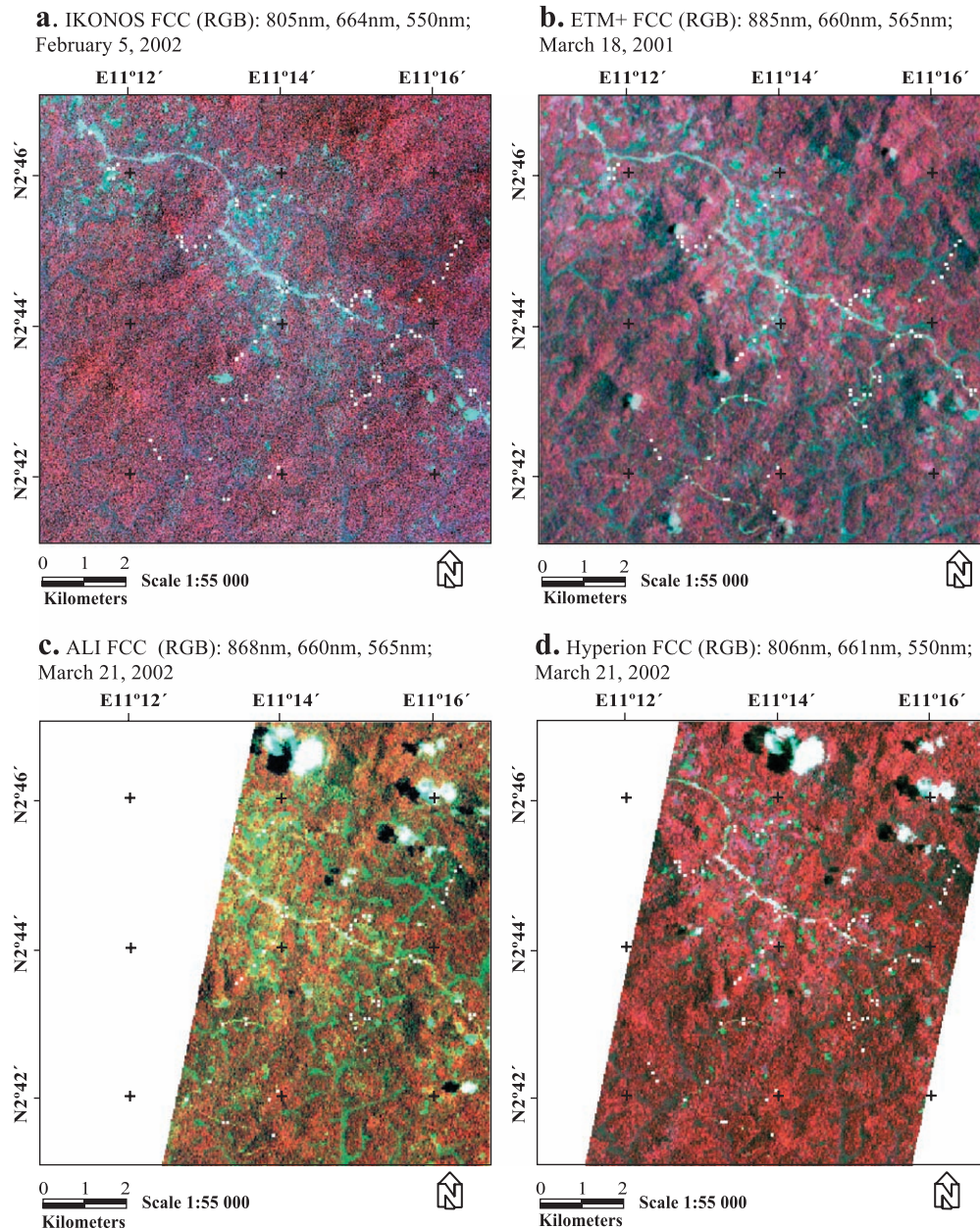


Fig. 1. The new generation satellite sensor images of the study area in the Congo River basin, southern Cameroon.



The study used remote sensing data and field data acquired over the summer months of February and March from the Congo basin rainforests in southern Cameroon (Fig. 1).

## 2. Methods—field data collection

### 2.1. Study area

The study area is located near the Akok village in southern Cameroon and is part of the Congo River basin. The new generation of images covering the study area is illustrated in Fig. 1. The Akok site was selected because it is still dominated by large tracts of intact tropical moist and semi-deciduous central African forests interspersed with fallow-agricultural lands and cocoa agroforests. Parts of the study area are also being exploited for timber at increasing rates. Thus, this study also provides an opportunity to examine the impacts of anthropogenic disturbances, such as slash-and-burn agriculture and logging, on rainforests near villages and road networks.

Precipitation averages 1513 mm annually over the study region (Hauser & Nolte, 2002) and has a bi-modal distribution, with most rain falling during April–May and August–October. February and March are usually the driest months. Using Walter's (1985) classification for forest types of the world, the area is largely covered by dense evergreen rain forest. The soil is an isohyperthermic Typic Kandiodult (Hauser & Nolte, 2002).

### 2.2. Field plot data

Field data were collected between March 6 and 16, 2002, to coincide with the Hyperion, ALI, and IKONOS image acquisitions (Table 1) and the peak of the dry season. Dry month imagery have been shown to reveal greater differences among vegetation types and land use because of variations in tolerance to water stress among vegetation types and differences in soil moisture availability among sites (Whitmore, 1998).

#### 2.2.1. Plot selection

Inventory field plots were 30 × 30-m quadrants. Each plot encompasses 52 IKONOS pixels but only a single Hyperion, ALI, and ETM+ pixel. Plots were established within large (i.e., at least 1 ha) homogeneous areas of class under consideration (e.g., young secondary forest), thus avoiding small patches of a particular LULC or vegetation class. This measure reduced any difficulty in registering to an exact pixel in the 30-m resolution data (Hyperion, Landsat, ALI). Our confidence in the accuracy of plot locations was enhanced by the availability of digital, georeferenced IKONOS images in the field. Each plot location was digitally recorded onto the IKONOS images right in the field.

Forest biotic variables were collected from 102 locations, of which 65 fell within all images (Table 2). These 65 plots

were located in primary forests (16 plots), secondary forest (36), and fallows (13). The other 37 plots were either outside one of the four images, masked by image interference (e.g., cloud), or were located in other LULC types (e.g., slash and burn farm). Within each plot, diameter at breast height (dbh) was measured for all tree and shrub stems with dbh greater than or equal to 10 cm. Also recorded within the plots were the six most dominant tree species, the six most dominant shrub species, the percent canopy cover, and the LULC category. Dominant tree and shrub species were ranked by stem basal area and stem density, respectively. Plots were established along transects running perpendicular to the least disturbed access paths. Transect locations were selected haphazardly and determined primarily by access.

In addition to the 65 detailed inventory plots, qualitative observations of LULC or forest cover were noted at 378 other locations and recorded directly onto the IKONOS images in the field using ERMMapper™ software and Global Positioning System (GPS) readings. The size of the 378 qualitative assessment plots varied widely depending on the homogeneity or heterogeneity of the landscape as observed in the field as well as on the image. The qualitative data were used to generate spectral profiles of LULC or forest cover classes (Fig. 2) and to identify and label spectral classes.

LULC classes included primary forests without evidence of anthropogenic disturbance (134 qualitative assessments) and degraded primary forest with some evidence of anthropogenic disturbance (54). Other LULC classes included young secondary forest between 9 and 15 years (15 qualitative assessments in IKONOS images; see Table 2), mature secondary forest between 15 and 40 years (6), and mixed secondary forest with significant anthropogenic disturbance and a mixture of young and old trees left standing after incomplete logging (15). Fallow LULC classes were agricultural lands recently abandoned with regrowth vegetation between 1 and 8 years (67). The two predominant agricultural LULC classes were agricultural-crop lands (8 qualitative assessments), and slash and burn (swidden) farms (7). Lowland wetland vegetation occurred mainly along stream courses and included *Raphia* palm and bamboo vegetation (29 qualitative assessments). *Piptadenia africana* (6 qualitative assessments) stands are a significant part of this forest. *P. africana* has low timber value, but grow to large sizes and may be important carbon sinks and components of forest biomass. Other LULC and vegetation categories included cocoa plantations (6 qualitative assessments), iselberg rocks (14), built-up areas (8) soccer fields (8), and dirt roads (1). The percent cover of each land cover types (e.g., trees, shrubs, grasses) was determined at each field plot. Each LULC had several field plots. Thereby, the percent cover of each LULC categories was determined based on filed plot data.

The vegetation types were classified based on the expert knowledge of one of the authors, who is a well-trained expert with several years of experience in African vegeta-

Table 2  
Distribution of tree, shrub, and weed species in the 30 × 30-m ground plots

LULC	Number of plots covered by each				Number <sup>a</sup> of tree species <sup>a</sup>	Total tree count <sup>a</sup>	Average dbh (cm)	Dominant tree species	Average area covered by tree species (%) <sup>b</sup>	Dominant shrub species	Average area covered by shrub species (%) <sup>b</sup>	Dominant weed species	Average area covered by weed species (%) <sup>b</sup>	Average dry weight tree biomass (kg m <sup>-2</sup> ) <sup>b</sup>
	ALI	Hyperion	IKONOS	ETM+										
Primary forest <sup>c</sup>	14	16	16	16										
(a) Pristine	12	13	13	13	45	68	28.4	<i>Piptadenia africana</i>	63.8	<i>Cissus</i> spp.	32.4	<i>Pteridium aquilinum</i>	0	116.6
(b) Degraded	2	3	3	3	10	11	23.2	<i>Discoglyprena caloneura</i>	56.3	<i>Lacospermas secundii</i>	35.3	<i>Megaphrenium</i> spp.	1.7	55.1
Secondary forest <sup>c</sup>	26	26	36	36										
(a) Young	10	8	15	15	37	76	32.4	<i>Piptadenia africana</i>	45.1	<i>Haumania delkelmaniana</i>	45.9	<i>Pteridium aquilinum</i>	2.2	56.4
(b) Mature	5	6	6	6	21	29	33.2	<i>Antrocaryon klaineianum</i>	46.8	<i>Alchornea floribunda</i>	39.8	<i>Megaphrenium</i> spp.	1.7	33.8
(c) Mixed	11	12	15	15	34	51	32.0	<i>Piptadenia africana</i>	39.1	<i>Lacospermas secundii</i>	46.4	<i>Pteridium aquilinum</i>	6.1	72.5
Fallow	9	10	13	13										
(a) 1–3 years	5	5	8	8	4	4	37.6	<i>Pycnantus angolensis</i>	2.6	<i>Alchornea cordifolia</i>	9.4	<i>Epatorium odoratum</i>	81.4	1.7
(b) 3–5 years	2	3	3	3	7	8	17.4	<i>Rauwolfia macrophylla</i>	10.3	<i>Elaeis guineensis</i>	85.7	<i>Aframomum giganteum</i>	1.7	3.1
(c) 5–8 years	2	2	2	2	7	9	17.8	<i>Alstonia congensis</i>	5.5	<i>Elaeis guineensis</i>	43.0	<i>Pteridium aquilinum</i>	2.5	3.3

The number of plots for each LULC category was used for deriving mean or average information.

<sup>a</sup> The number of tree species and counts were average from all plots falling in the respective LULC category.

<sup>b</sup> Average area covered is for dominant tree species.

<sup>c</sup> Description of each sub-class is provided in Section 2.2.1.



Fig. 2. Nine rainforest land use/land cover classes selected for forest classification.

tion, specially that of Cameroon. The age classes were also determined by the same vegetation expert. The LULC classes were based on USGS Anderson scheme (Anderson et al., 1976). The secondary regrowth in the area can be easily grouped into age categories (e.g., 1–3 year fallow, 3–5 year fallow, and so on) through local knowledge of vegetation growth patterns. The ages of older trees were determined as estimates (rather than precise age).

Spectral data on LULC and forest cover classes were extracted from 480 locations (102 detailed inventory plots plus 378 LULC qualitative assessment plots, excluding points masked by cloud cover or falling outside an image). The specific locations of all sites were recorded using an e-trek palm-held Garmin™ GPS unit.

#### 2.2.2. Plot description

The LULC classifications were made in the field based on (a) knowledge of the local vegetation dynamics; (b) presence or absence of disturbance (anthropogenic or otherwise); and (c) percent canopy cover. Summary statistics

on the species and diameter distributions of the different LULC classes are provided in Table 2. The dominant tree species in terms of canopy cover and basal area per plot were *P. africana* and *Discoglypremna caloneura*. The high biomass ( $\text{kg m}^{-2}$ ) capacity of pristine primary forests relative to other forests types (Table 2) highlights the importance of these forests for the purposes of carbon sequestration and timber production. The dominant shrub species in terms of canopy cover per plot occupy about one-third to one-half of the plot area.

#### 2.2.3. Biomass allometry

For biomass measurements, seven 1–3-ha plots were selected where farmers had recently (within the previous 2 days) felled the trees and cleared all other vegetation. Plots selection criteria included (a) spatial location within the study area; (b) date of felling or clear cutting (within the last 2 days); and (c) availability of tree species within the plot. Farmers traditionally burn all felled vegetation, including the trees, within a few days of clearing. We identified felled

but unburned sites and requested access to these sites for biomass measurements from the resident farmers.

Biomass measurements were made by taking wood samples at different heights of the trees, as well as in branches. The estimated volumes of the wood samples along with their weights were used to calculate wood density ( $\text{kg m}^{-3}$ ). The fresh weight biomass of an entire tree ( $\text{kg tree}^{-1}$ ) was then estimated. Sampling was carried out on a wide range of species to develop allometric equations relating tree fresh weight biomass ( $\text{kg tree}^{-1}$ ) to dbh. The samples were then oven-dried for 2 weeks at  $70^\circ\text{C}$  to relate dry weight biomass to dbh. The dbh values of each tree were then used to predict tree dry weight biomass ( $\text{kg tree}^{-1}$ ; Fig. 2b). Dry weight biomass predictions from this study were similar ( $R^2=0.99$ ; Fig. 3b) to predictions obtained from the United Nations Food and Agricultural Organization (FAO) equations for tropical rainforests (Brown, 1997).

Dry weight biomass per unit plot area ( $\text{kg m}^{-2}$ ) was derived by simple addition of:

- (A) *Large tree and shrub biomass*: total predicted dry weight biomass ( $\text{kg tree}^{-1}$ ) of all trees and shrubs  $\geq 10$  cm dbh, divided by plot area ( $900 \text{ m}^2$ ).
- (B) *Weed, grass, and small tree and shrub biomass*: for trees and shrubs  $< 10$  cm dbh, weeds, and grasses we used the

dry weight biomass ( $\text{kg m}^{-2}$ ) estimates for African rainforests from Nolte and Hauser (2002). In LULC classes other than primary and secondary forests, the grasses, crops, and weeds were significant components of plot biomass. In these plots, dry weight biomass ( $\text{kg m}^{-2}$ ) was obtained by cutting a representative  $1 \times 1\text{-m}$  subplot, then drying and weighing the vegetation. The area was considered “representative” if the vegetation in the  $1 \times 1\text{-m}$  subplot appeared similar to the surrounding area in terms of vegetation vigor, cover, and height.

### 3. Methods—image processing

#### 3.1. Data sets

All images were acquired in February or March (Fig. 1). The Hyperion and ALI images were acquired on March 21, 2002, while the IKONOS image was acquired approximately a month earlier (February 5, 2002). No suitable ETM+ images from summer 2002 were available; hence, an ETM+ image was acquired for the previous summer (March 18, 2001).

The four spaceborne sensors used in this study (Table 1) offer the most advanced spectral, spatial, and radiometric characteristics commercially available for the general public. In this study, we used 4 spectral channels from the IKONOS sensor, 6 non-thermal ETM+ bands, 9 multispectral ALI bands, and 157 of the 242 Hyperion narrowbands. Of the original 242 Hyperion bands, 196 were unique and calibrated: bands 8 (427.55 nm) to 57 (925.85 nm) from the visible and near-infrared (VNIR) sensors; and bands 79 (932.72 nm) to 224 (2395.53 nm) from the SWIR sensors. The redundant and uncelebrated bands were in the 357–417, 936–1068, and 852–923 nm ranges. In addition, initial spectral profiles showed high levels of noise and/or poor signals in the Hyperion data over the 1306–1437, 1790–1992, and 2365–2396 nm ranges; bands spanning these portions of the spectrum were therefore dropped.

#### 3.2. Image rectification and registration

Prior to the field work, 22 ground control points (GCPs) were collected at clear landmarks (e.g., road intersections, bridges) throughout the IKONOS images. These GCPs were used to rectify the IKONOS image (root mean square error  $< 1$  pixel/4 m). The Hyperion, ETM+, and ALI images were then registered to the rectified IKONOS image with root mean square errors below 1 pixel.

#### 3.3. Normalization

The Hyperion, IKONOS, ALI, and ETM+ sensors have different radiometric resolutions (Table 2), hence their respective digital numbers (DNs) carry different levels of information and cannot be directly compared. Therefore,

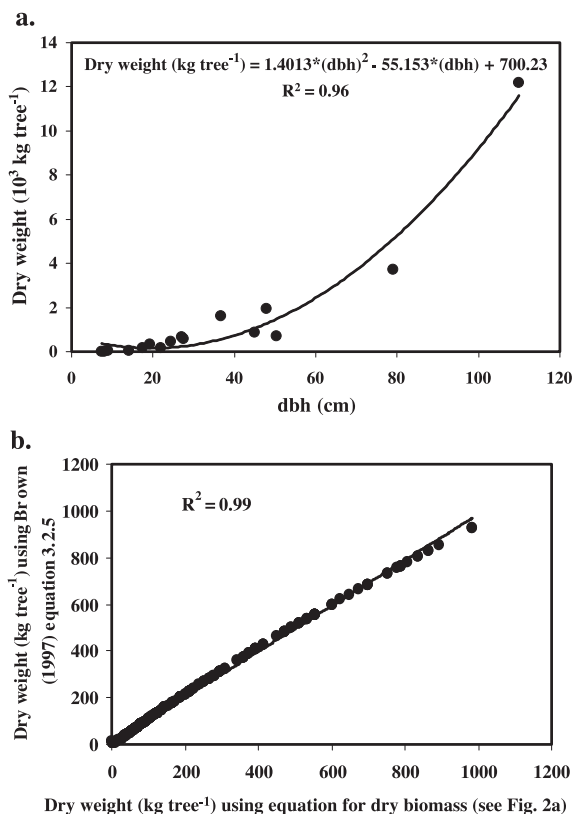


Fig. 3. Allometric dry weight biomass equation development (a) Allometric dry weight biomass equation ( $n=16$  tree species) (b) Linear correlation of dry biomass estimates using dry biomass equation (this study see Fig. 2a) and FAO equation 3.2.5 (Brown, 1997).



they were converted to absolute units of radiance ( $\text{W m}^{-2} \text{sr}^{-1} \mu\text{m}^{-1}$ ), then to apparent at-satellite reflectance (%), and finally to surface reflectance (%) after atmospheric correction. Details on these conversions are provided due to the uniqueness of the sensors involved.

### 3.3.1. Hyperion data to radiance

The DNs of the Hyperion level 1 products are 16-bit radiances and are stored as 16-bit signed integers. The DNs were converted to radiances ( $\text{W m}^{-2} \text{sr}^{-1} \mu\text{m}^{-1}$ ) using an appropriate scaling factor: 40 for visible and VNIR, and 80 for SWIR. Hence,

$$\text{Radiance (W m}^{-2} \text{sr}^{-1} \mu\text{m}^{-1}) \text{ for VNIR bands} = \frac{\text{DN}}{40}, \quad (1)$$

and

$$\text{Radiance (W m}^{-2} \text{sr}^{-1} \mu\text{m}^{-1}) \text{ for SWIR bands} = \frac{\text{DN}}{80}. \quad (2)$$

### 3.3.2. IKONOS data to radiance

The 11-bit IKONOS DNs were converted to radiance ( $\text{m W cm}^{-2} \text{sr}^{-1}$ ) using the equation

$$L_{ij} = \text{DN}_{ij} \times [\text{CalCoef}_j]^{-1}, \quad (3)$$

where  $L_{ij}$  and  $\text{DN}_{ij}$  are the in-band radiance at sensor aperture ( $\text{mW cm}^{-2} \text{sr}^{-1}$ ) and image product digital value of the  $i$ th pixel in the  $j$ th band, respectively, and  $\text{CalCoef}_j$  is the in-band radiance calibration coefficient ( $\text{DN cm}^2 \times \text{sr m}^{-1} \text{W}^{-1}$ ). Since the IKONOS image used in this study was acquired after February 22, 2001, the values of  $\text{CalCoef}_k$  used were 728 for band 1, 727 for band 2, 949 for band 3, and 843 for band 4 (see [Space Imaging, 2001](#)).

### 3.3.3. ALI data to radiance

The DNs of the ALI sensor represent 16-bit absolute radiances but are stored as 16-bit integers with a scaling factor of 300. Therefore, the ALI DNs were converted to radiances ( $\text{mW cm}^{-2} \text{sr}^{-1}$ ) using the equation:

$$\text{Radiance (mW cm}^{-2} \text{sr}^{-1}) \text{ for ALI} = \frac{\text{DN}}{300}. \quad (4)$$

### 3.3.4. ETM+ data to radiance

The ETM+ 8-bit DNs were converted to radiances using the equation:

$$\text{Radiance (W m}^{-2} \text{sr}^{-1} \mu\text{m}^{-1}) = \text{gain} \times \text{DN} + \text{offset}, \quad (5a)$$

This can also be expressed as:

$$\begin{aligned} \text{Radiance (W m}^{-2} \text{sr}^{-1} \mu\text{m}^{-1}) = & \frac{\text{LMAX} - \text{LMIN}}{\text{QCALMAX} - \text{QCALMIN}} \\ & \times (\text{QCAL} - \text{QCALMIN}) \\ & + \text{LMI}, \end{aligned} \quad (5b)$$

where  $\text{QCALMIN}=1$ ,  $\text{QCALMAX}=225$ ,  $\text{QCAL}$  is the digital number,  $\text{LMIN}$  and  $\text{LMAX}$  are the spectral radiances

for each band at DNs 1 and 255 (i.e.  $\text{QCALMIN}$ ,  $\text{QCALMAX}$ ), respectively. The  $\text{LMAX}$  and  $\text{LMIN}$  values ( $\text{W m}^2 \text{Sr} \mu\text{m}$ ) for the March 18, 2001, ETM+ image are:  $\text{LMAX}_{\text{band1}} = 191.600$ ;  $\text{LMIN}_{\text{band1}} = -6.200$ ;  $\text{LMAX}_{\text{band2}} = 196.500$ ;  $\text{LMIN}_{\text{band2}} = -6.400$ ;  $\text{LMAX}_{\text{band3}} = 152.900$ ;  $\text{LMIN}_{\text{band3}} = -5.000$ ;  $\text{LMAX}_{\text{band4}} = 241.100$ ;  $\text{LMIN}_{\text{band4}} = -5.100$ ;  $\text{LMAX}_{\text{band5}} = 31.060$ ;  $\text{LMIN}_{\text{band5}} = -1.000$ ;  $\text{LMAX}_{\text{band61}} = 17.040$ ;  $\text{LMIN}_{\text{band61}} = 0.000$ ;  $\text{LMAX}_{\text{band62}} = 12.650$ ;  $\text{LMIN}_{\text{band62}} = 3.200$ ;  $\text{LMAX}_{\text{band7}} = 10.800$ ;  $\text{LMIN}_{\text{band7}} = -0.350$ ;  $\text{LMAX}_{\text{band8}} = 243.100$ ;  $\text{LMIN}_{\text{band8}} = -4.700$ .

### 3.3.5. Radiance to reflectance

A reduction in between-scene variability can be achieved through a normalization for solar irradiance by converting spectral radiance, as calculated above, to planetary reflectance or albedo ([Markham & Barker, 1985, 1987](#)). This combined surface and atmospheric reflectance of the Earth is computed with the following formula:

$$\rho_p = \frac{\pi L_\lambda d^2}{\text{ESUN}_\lambda \cos \theta_s}, \quad (6)$$

where  $\rho_p$  is the at-satellite exo-atmospheric reflectance,  $L_\lambda$  is the radiance ( $\text{W m}^{-2} \text{sr}^{-1} \mu\text{m}^{-1}$ ),  $d$  is the earth to sun distance in astronomic units at the acquisition date (see [Markham & Barker, 1987](#)),  $\text{ESUN}_\lambda$  is the mean solar exo-atmospheric irradiance ( $\text{W m}^{-2} \text{sr}^{-1} \mu\text{m}^{-1}$ ) or solar flux ([Neckel & Labs, 1984](#)), and  $\theta_s$  is solar zenith angle in degrees (i.e.,  $90^\circ$ ; minus the sun elevation or sun angle when the scene was recorded as given in the image header file).

### 3.3.6. Surface reflectance

Atmospheric correction was performed using the improved dark object subtraction technique ([Chavez, 1986, 1996](#)) to derive surface reflectance from apparent reflectance.

## 4. Methods—image data analysis

We implemented a series of unique methods and techniques in modeling biomass and classifying hyperspectral, hyperspatial, and advanced multispectral data sets. These methods are discussed below.

### 4.1. Models with rigorous search criterion or data mining

Adjacent wavebands often contain redundant information. The original, high-dimensional data sets were therefore distilled by removing the redundant bands and keeping only those that contained most of the information. This was achieved by lambda-by-lambda  $R^2$  contour plots or through principal component analysis (PCA).



#### 4.1.1. Contour plots of Hyperion bands

Lambda-by-lambda  $R^2$  contour plots of Hyperion bands (LLR<sup>2</sup>PHBs) are obtained from the matrix of bivariate  $R^2$  values. For the Hyperion data set, the 157 band by 157 band  $R^2$  matrixes (24,649  $R^2$  values) was calculated for each LULC or forest cover class (e.g., primary forest). Two highly correlated wavebands indicate a redundancy in that they are providing similar information. From this, the least redundant bands are those with the least  $R^2$  values.

#### 4.1.2. Principal component analysis of Hyperion

Principal component analysis of Hyperion (PCAH) involved a factor analysis in which the proportion of the total variability in the data set explained by each principal component (PC) was established by its corresponding eigenvalue. The relative contribution of each Hyperion waveband to a PC is indexed by the band's factor loading in the corresponding eigenvector.

#### 4.1.3. Two-band Hyperion vegetation index

Two-band Hyperion vegetation indices (TBHVI) (see Thenkabail et al., 2000a) were calculated according to the following equation:

$$\text{TBHVI}_{ij} = \frac{(R_j - R_i)}{(R_j + R_i)}, \quad (7)$$

where  $R_i$  and  $R_j$  are the reflectances in Hyperion narrow-bands  $i$  and  $j$ . A total of 24,649 TBHVIs were computed for the Hyperion data set, and these were related to dry weight biomass estimates ( $\text{kg m}^{-2}$ ). Wavebands incorporated into the TBHVIs that predicted dry weight biomass (in terms of  $R^2$  values) were retained.

#### 4.1.4. Derivative greenness Hyperion vegetation index

Derivative greenness Hyperion vegetation indices (DGHVIs; see Elvidge & Chen, 1995) were computed from Hyperion spectra in regions of rapid change in slope of spectra per unit change in wavelength:

$$\text{DGVI} = \sum_{\lambda_1}^{\lambda_n} \frac{[\rho(\lambda_1) - \rho(\lambda_j)]}{\Delta\lambda_i}, \quad (8)$$

where  $\lambda_i$  and  $\lambda_j$  are the wavelengths at the midpoints of bands  $i$  and  $j$ ,  $\rho$  is the first derivative of the reflectance,  $\tilde{e}_1$  is the start of a DGVHI waveband, and  $\tilde{e}_n$  is end of a DGHVI waveband. The regions for rapid change in Hyperion spectra ( $\tilde{e}_1$  and  $\tilde{e}_2$ ) were taken to be 509–539, 539–560, 560–580, 651–672, 702–743, 621–794, 1498–1649, 2083–2355, 428–906, and 428–2355 nm. DGHVI values determined from these regions were consecutively named DGHVI1 through DGHVI10 and were related to forest biomass estimates ( $\text{kg m}^{-2}$ ).

#### 4.1.5. Optimum multiple band Hyperion vegetation index

Optimum multiple band Hyperion vegetation indices (OMBHVI) were computed using:

$$\text{OMBVI}_i = \sum_{j=1}^N a_{ij} R_j, \quad (9)$$

where  $\text{OMBVI}_i$  is the OMBVI for the  $i$ th LULC variable,  $R_j$  is the reflectance in the  $j$ th band, and  $a_{ij}$  is the coefficient for reflectance in band  $j$  for the  $i$ th LULC variable. The model was run in SAS Institute (1999) using the stepwise MAXR procedure (Thenkabail, 2002).

#### 4.1.6. Broadband vegetation index

Broadband vegetation indices (BBVIs) were computed for the IKONOS, ETM+, and ALI sensor data using the procedures described in Sections 4.1.3 and 4.1.5. The only difference is that the matrices involved are much smaller.

#### 4.2. Discrimination or separability analysis

Spectral separability of LULC classes was achieved using a stepwise discriminant analysis (SDA) approach that involved Wilks' Lambda. The SDA (Draper & Smith, 1981, Chapter 6) was performed using the PROC STEPDISC algorithm in SAS Institute (1999) and involved a stepwise selection (Klecka, 1980) of wavebands from the Hyperion, ALI, ETM+, and IKONOS data sets. The stepwise selection process began with no variables in the model. At each step, the variable that contributed the most to the discriminatory power of the mode was added and, if one or more variables in the model failed to meet the retention criterion, the variable contributing the least was removed. When all variables in the model met the retention criterion, and no other variables meet the criteria to enter the model, the stepwise selection process stops.

The SDA is based on Wilks' Lambda. Wilks' Lambda is indicative of the discriminatory power of the model and is one of the test statistics preferred for multivariate analysis of variance (MANOVA) (Townend, 2002). Wilks' Lambda is calculated as:

$$\text{Wilk's } \Lambda = \prod_{i=1}^k \frac{1}{1 + \lambda_i}, \quad (10)$$

where  $\lambda_i$  is the  $i$ th eigenvalue of  $\tilde{E}W^{-1}$ ,  $W$  is the pooled "sum-of-squares (SS)" and cross-products matrices and

$$\Lambda = \frac{|S_{\text{error}}|}{|S_{\text{effect}} + S_{\text{error}}|}, \quad (11)$$

is a ratio of the matrix determinants of ( $S_{\text{error}}$ ) and ( $S_{\text{effect}}$ ), where  $S$  is a matrix also known as "sum of squares (SS) and cross-products.

#### 4.3. Discriminant model to classify forest biotic variables and assess their accuracy

PROC DISCRIM (SAS Institute, 1999) develops a discriminant model that can be used to classify each pixel into one of the LULC or forest cover classes such as primary forest, secondary forest, and fallows. The discriminant model, also known as a classification criterion, is determined by a measure of generalized squared distance (Rao, 1973). The classification criterion can be based on either the individual within-group covariance matrices or the pooled covariance matrix; it also takes into account the prior probabilities of the groups. Each observation is placed in the class from which it has the smallest generalized squared distance. The procedure, as it is implemented in SAS, can also compute the posterior probability of an observation belonging to each class.

The generalized squared distance ( $D$ ) function for LULC classes is:

$$D_j^2(X) = (X - \bar{X}_j) \text{COV}^{-1} (X - \bar{X}_j) \quad (12)$$

where,  $X$  is the vector of observations for a given pixel,  $\bar{X}_j$  is the mean vector over all pixels in LULC class  $j$ , and COV is the covariance matrix. The posterior prob-

ability of membership for pixel  $X$  across all LULC classes  $j$  is:

$$Pr(j | X) = \exp[-0.5D_j^2(X)] / \sum_k \exp[-0.5D_k^2(X)] \quad (13)$$

PROC DISCRIM (SAS Institute, 1999) will determine classification accuracies for various combinations of wavebands. The procedure was used to determine the accuracies of forest classifications based on various combinations of wavebands from the IKONOS, ETM+, ALI, and Hyperion sensors.

## 5. Results and discussion—use of images to predict biomass

### 5.1. Spectral profiles of the normalized data

Examination of average reflectance spectra (see Fig. 4) for different vegetation types indicated that the Hyperion data provided many possibilities for separating vegetation categories using specific narrowbands throughout the 600–2350-nm spectral range. The IKONOS sensor provided

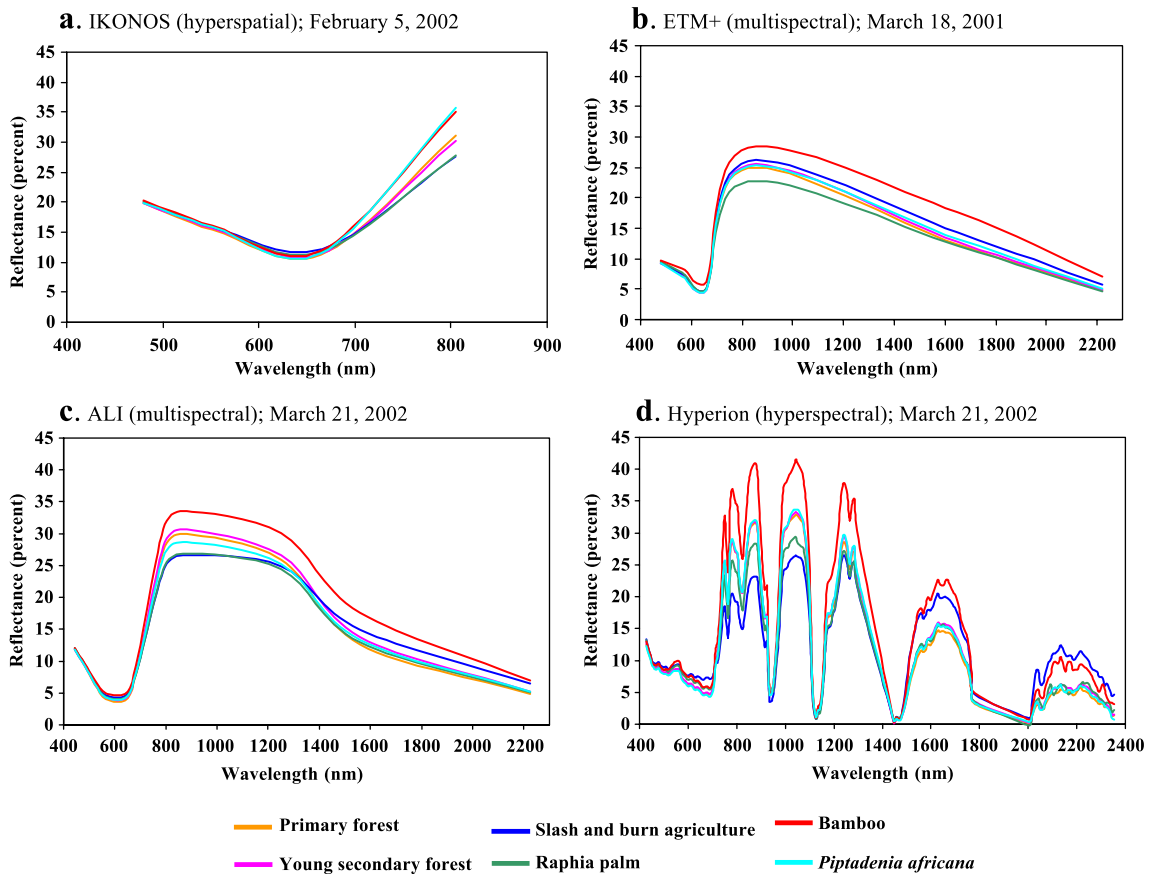


Fig. 4. Mean spectral profile of rainforest vegetation using (a) hyperspatial; (b and c) advanced multispectral; and (d) hyperspectral sensors.

separability in a single near infrared (NIR) broadband, and the ETM+ and ALI sensors in a few NIR and MIR bands.

## 5.2. Data mining for redundant and prominent wavebands

### 5.2.1. Lambda versus Lambda $R^2$ contour plots

Direct correlations of Hyperion reflectance data in the 400–2500-nm region were established from a pooled data set that included all primary forest, secondary forest, and fallow classes. The correlations were converted to  $R^2$  values. A contour plot of  $R^2$  values (as shown in Fig. 5) in  $\lambda_1$  (157 useful Hyperion bands) by  $\lambda_2$  (157 bands) helped separate redundant bands from non-redundant bands. The lower the  $R^2$  value, the greater the non-redundancy or higher the information uniqueness between bands, leading to a ranking of these non-redundant bands. The regions with high  $R^2$  values are information of redundant regions and are left blank. The results help in separating the redundant versus non-redundant Hyperion wavebands. The outcome will lead to identifying least redundant bands and ranking them.

### 5.2.2. Principal component analysis

The results for the principal component analyses for each sensor, across all vegetation types, are provided in Table 3. Due to the existence of only four broadbands, a

high proportion of the variability (97.7%) in the IKONOS data set was explained by the first two PCs alone. Similarly, the first two PCs explained a high proportion of the variability in the ETM+ (85.8%) and ALI (92.7%) data sets. In contrast, only 64.9% of the variability in the Hyperion data set was explained by the first two PCs, due in part to the much larger number of wavebands. The first 23 PCs were needed to explain 94.7% of the variability in the Hyperion data set. Relative to the broadband sensors, finer levels of detail and more subtle changes in the landscape are captured by the Hyperion sensor. It needs to be noted that the importance of lower-order PCs is of crucial importance for gathering certain unique information (e.g., species types) even if they explain only a small proportion of the variability.

The Hyperion results in Table 3 show that the wavebands that had the highest weighting on PC1 were predominantly early mid-infrared (EMIR; 1300–1900 nm) bands followed by far near infrared (FNIR; 1100–1300 nm) bands. Far mid-infrared (FMIR; 1900–2350 nm) and red (600–700 nm) wavebands dominated PC2. Since PC1 and PC2 explain most of the variability, the wavebands that dominate in PC1 and PC2 are the most important. Remarkably, MIR bands are the most prominent wavebands in PC1, and have significant presence in PC2, for the narrowband

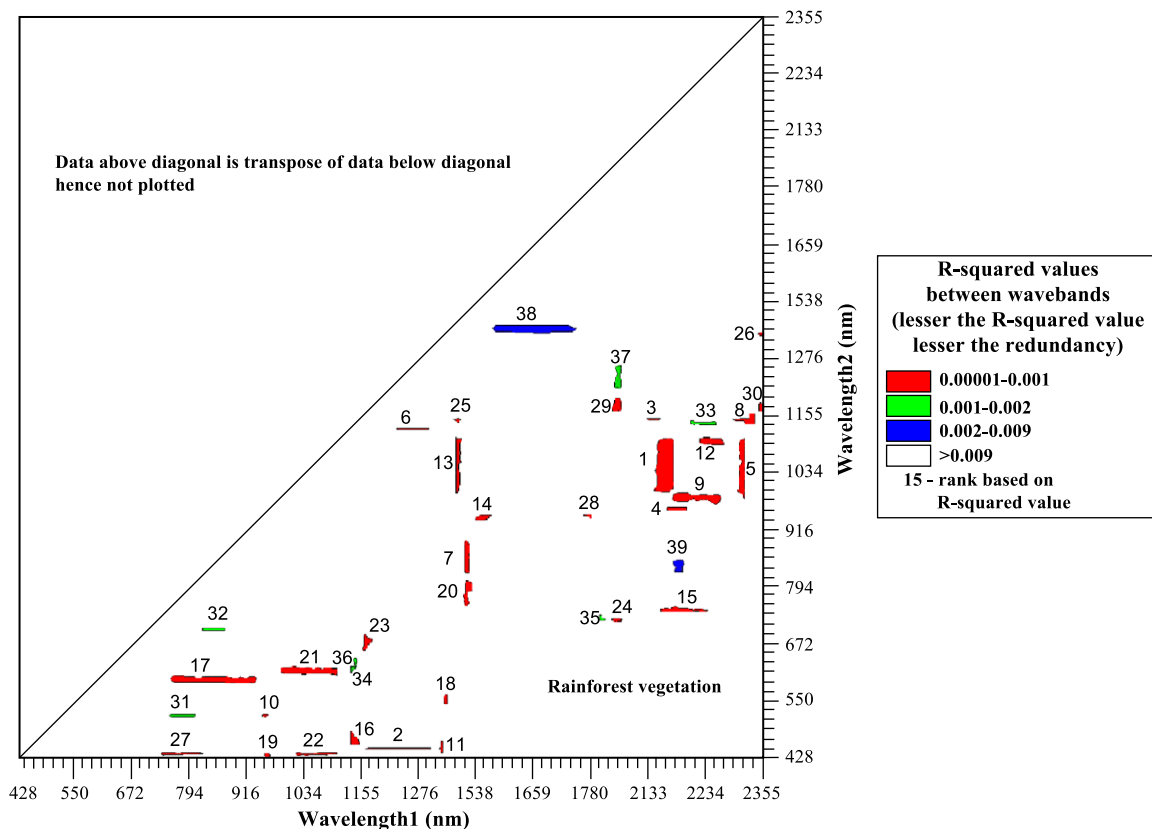


Fig. 5. Lambda-by-lambda  $R^2$  contour plot based on 157 Hyperion bands showing least redundant bands (marked areas) and most redundant bands (blank areas). Rainforest vegetation includes primary forest, secondary forest, and fallow LULC classes.

Table 3  
Highest loaded wavebands for principal components 1 to 5 for each sensor

Sensor	Wavebands <sup>a</sup>	PC1 <sup>b</sup>	Wavebands <sup>a</sup>	PC2 <sup>b</sup>	Wavebands <sup>a</sup>	PC3 <sup>b</sup>	Wavebands <sup>a</sup>	PC4 <sup>b</sup>	Wavebands <sup>a</sup>	PC5 <sup>b</sup>	PC1 + PC2 <sup>b</sup>
IKONOS	b665 b551 b480 b805	73.9	b805 b480 b551 b665	23.8	b665 b551 b805 b480	1.6	b665 b805 b480 b551	0.7	not applicable	not applicable	97.7
Landsat 7-ETM +	b1650 b2220 b565 b660 b482	66.1	b825 b1650 b565 b482 b2220	19.7	b660 b565 b825 b1650 b2220	7.3	b565 b660 b482 b825 b2220	4.0	b660 b825 b482 b1650 b2220	2.5	85.8
ALI	b2225 b483 b443 b565 b660	68.6	b868 b790 b1250 b1560 b2225	24.1	b443 b483 b868 b790 b660	3.5	b565 b660 b2225 b1250 b868	2.0	b483 b1560 b790 b660 b565	1.1	92.7
Hyperion	b1659 b1669 b1649 b1720 b1639 b1578 b1699 b1689 b1679 b1588 b1710 b1730 b1619 b1629 b1609 b1760 b1599 b1568  b1750 b1740 b1548 b1558 b1538 b1770 b1528 b712 b1518 b1266 b1256 b1316 b1286 b1276 b722 b1245 b1185 b1235 b1215 b1175 b1225	46.9	b2032 b2022 b672 b682 b661 b692 b651 b2103 b2042 b2052 b631 b641 b2113 b509 b611 b590 b2123 b621 b2083 b489 b2285 b2234 b2153 b2264 b2143 b2325 b2073 b580 b499 b2224 b2093 b2194 b2305 b468 b478 b600 b519 b227	18.0	b1387 b1427 b1417 b1367 b1377 b2002 b1911 b2345 b2204 b2012 b1356 b2254 b1437 b2153 b2163 b2315 b2184 b1972  b1447 b2093 b2123 b2305 b1518 b2143 b1498 b2133 b2214 b2244 b2194 b2083 b1901 b2234 b1962 b2385 b2325 b2103 b1508 b1528	4.5	b1841 b1871 b1932 b1851 b1921 b1972 b1861 b1346 b1962 b1336 b1467 b1457 b1810 b1427 b1800 b2385 b1417 b2396  b1114 b2254 b1367 b458 b1124 b2244 b933 b895 b943 b2315 b489 b2093 b1780 b814 b1790 b682 b2305 b2325 b651 b1770 b1356	3.1	b1901 b1911 b1972 b1962 b1356 b2345 b2355 b1932 b1831 b1346 b1921 b1407 b1367 b1821 b1397 b1124 b2163 b1871  b1145 b1336 b1861 b478 b428 b2295 b1114 b448 b560 b1942 b529 b2254 b611 b1134 b2285 b702 b519 b1155 b600 b722 b1296	2.5	64.9 (94.7% for PC1 to PC23)
Dominating Hyperion wavebands	EMIR, FNIR, red-edge		FMIR, RED, blue		EMIR, FNIR		EMIR, FMIR, NIR		EMIR, FMIR		

<sup>a</sup> Wavebands providing highest factor loadings in order of ranking. Wavebands are ranked from left to right, then up/down.

<sup>b</sup> Percent of variability in data set explained.



Hyperion and broadband ETM+ and ALI data sets. IKONOS does not have MIR bands, therefore other wavebands dominate its PC1. However, a red band has the highest loading for the IKONOS PC1 and numerous red bands are present in the Hyperion PC2. This is a further confirmation of the importance of MIR bands in the remote sensing of rainforest vegetation (Boyd & Duane, 2001; Thenkabail et al., 1994). Lambert et al. (1995) clearly demonstrated that MIR bands show the greatest ability to discriminate between lightly and heavily damaged forest classes, and can also be applied to agroforests. A recent study by Thenkabail et al. (in press) demonstrated that the ETM+ bands in MIR helped explain about 20% more variability in forest biotic characteristics when compared to IKONOS. The potential of these bands has been recognized with the inclusion of MIR bands in many new generation sensors such as MODIS (1628–2155  $\mu\text{m}$ ), ASTER (1.6–2.43  $\mu\text{m}$ ), ETM+ (1.55–1.75 and 2.08–2.35  $\mu\text{m}$ ), IRS-1D (1.55–1.70  $\mu\text{m}$ ), and SPOT 4 (1.58–1.75  $\mu\text{m}$ ).

### 5.2.3. Two-band Hyperion vegetation indices (TBHVI)

The TBHVI were computed for every possible pair of Hyperion bands and related to dry weight biomass ( $\text{kg m}^{-2}$ ). Contour plots of the resulting  $R^2$  values were plotted on one side of the diagonal (the plots are symmetric about the diagonal) for primary forest (Fig. 6, above diagonal),

secondary forest (Fig. 6, below diagonal), fallows (Fig. 7, below diagonal), and the pooled data for all rainforest vegetation (Fig. 7, above diagonal). Contour plots are based on a nonlinear exponential relationship between TBHVI and dry weight biomass; this relationship consistently provided the fine fit across all vegetation types. The models were characterized by  $R^2$  values of approximately 0.7 for primary forest (Fig. 6), 0.6 for secondary forest (Fig. 6), 0.9 for fallows (Fig. 7), and 0.6 for these three classes combined (Fig. 7). Rankings of the band combinations provided in the models are in Figs. 6 and 7 and indicate which wavebands are best for modeling forest biomass. Regions with weak correlations indicate redundant wavebands.

### 5.3. Frequently occurring wavebands and the most sensitive maximal Hyperion wavebands

The 23 Hyperion bands listed in Table 4 (see also Fig. 8) comprise four bands in each of the EMIR, FMIR, and FNIR portions of the spectrum, three bands in each of the NIR (760–940 nm), red (600–700 nm), and moisture sensitive NIR (MSNIR; 940–1100 nm) spectral regions, and one band in each of the red-edge (700–740 nm) and blue (400–500 nm) portions of the spectrum. Previous studies using broadband sensors (e.g., Jakubauskas & Price, 1997) have established that biotic factors relating to the physical struc-

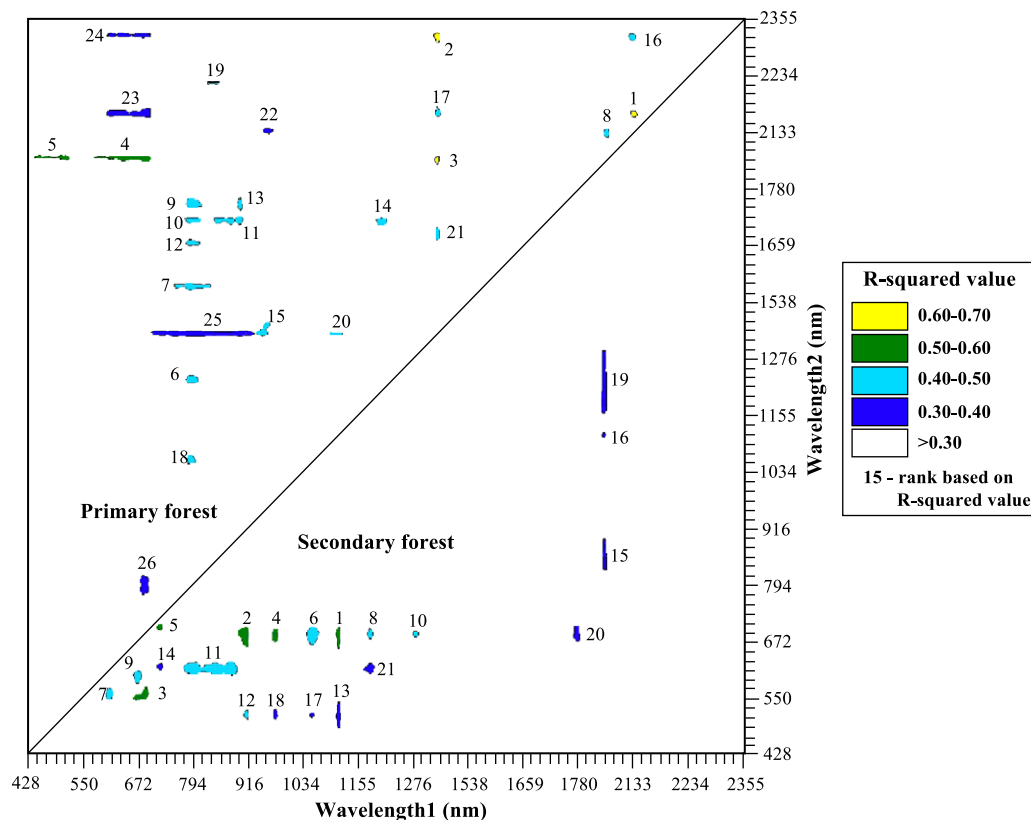


Fig. 6. Contour plots of  $R^2$  values for prediction of dry weight biomass from individual Hyperion bands using a nonlinear exponential model for (a) secondary forest (lower diagonal), and (b) primary forest (upper diagonal).

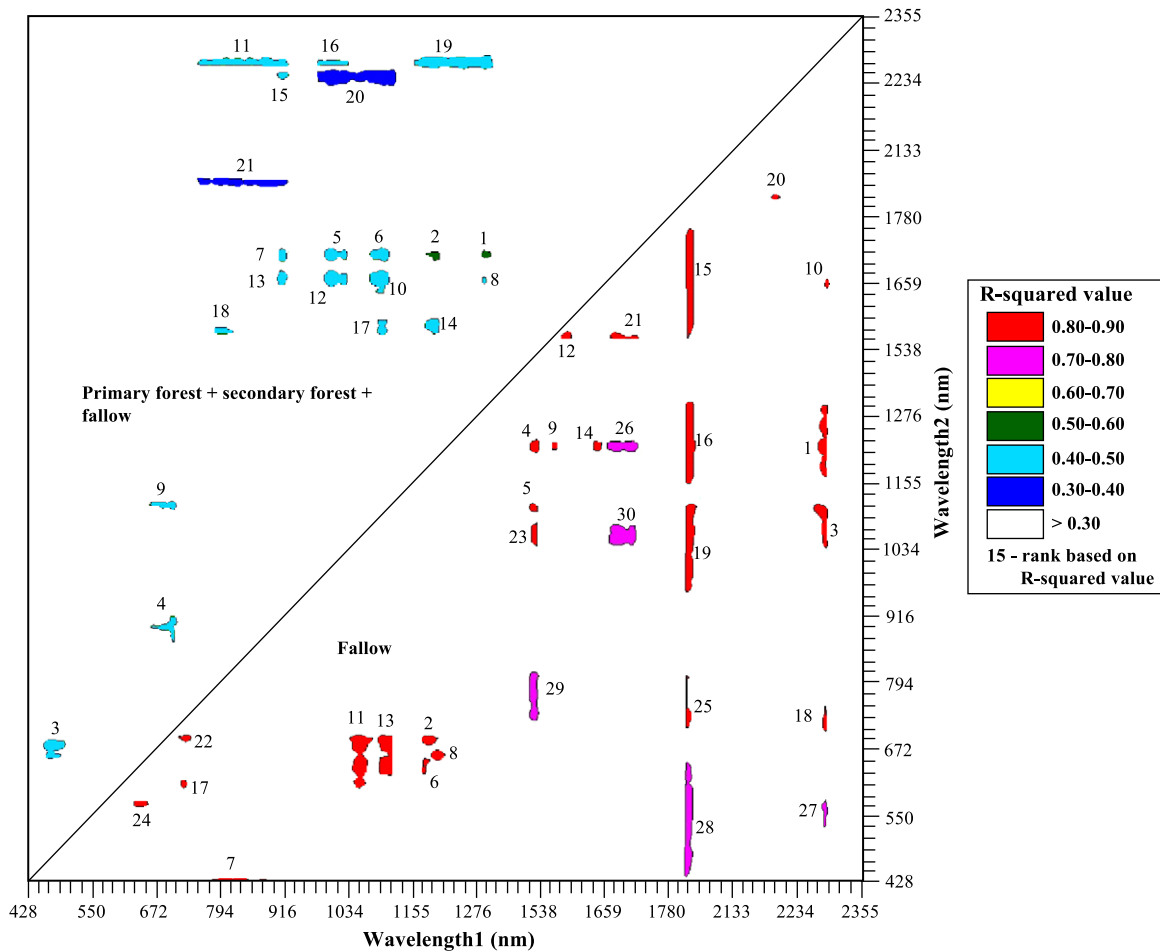


Fig. 7. Contour plots of  $R^2$  values for prediction of dry weight biomass from individual Hyperion bands using a nonlinear exponential model for (a) fallows (lower diagonal), and (b) all rainforest vegetation (upper diagonal).

ture of the forest canopy (e.g., height, basal area, biomass, and LAI) are predicted using MIR bands (TM5 and TM7) or a combination of visible (TM1, TM2, or TM3) and MIR bands. The spectral differences between two forest types are most pronounced in TM bands 4 (NIR) and 5 (MIR) where forests of comparable biomass have different canopy geometry (Brondizio et al., 1996).

The Hyperion wavebands that were most sensitive in predicting forest biomass were identified based on  $R^2$  value thresholds (Figs. 6 and 7). The waveband combinations for primary forest, secondary forest, fallow, and overall are listed in Table 4. The two most frequently occurring wavebands were centered at 682 nm (Hyperion band 33) and 1710 nm (Hyperion band 156). In earlier studies using handheld spectroradiometers, Thenkabail et al. (2000a, 2002) determined that narrowbands near 675 and 680 nm were optimal for agricultural crop classification. The present study re-affirms the importance of using bands near 680 nm, which is within a maximal absorption region for vegetation. Starch, a polysaccharide of D-glucose, is the main food storage molecule of plants and has significant absorption near 1710 nm (Kumar et al., in press), in the

EMIR. These two bands are followed in the ranking by two other MIR bands: an EMIR band centered at 1467 nm and a FMIR band centered at 2052 nm (Table 4). The region around 1467 nm (Hyperion band 132) is a classic water absorption band as a result of lignin, cellulose, and starch (Fig. 8). The 2052-nm FMIR band (Hyperion band 190) is in protein absorption region. Lignin also has a broad absorption region spanning 2050–2140 nm (Kumar et al., in press). The relationship between leaf water content and leaf reflectance is linear around 2052 nm (Olson, 1967). Other important Hyperion bands in the FNIR are located around 1215 nm (Hyperion band 107) and 1104 nm (Hyperion bands 95 and 96). The region around 1215 nm is one of the prime water absorption regions in 400–2500-nm portion of the spectra. The FNIR region is one of the most neglected, yet promising regions; the FNIR is dominated by C–H stretch second overtones, features common to all biochemical constituents (Kumar et al., in press).

The NIR bands are crucial in developing spectral vegetation indices such as the widely used normalized difference vegetation index (NDVI). The two most frequently occurring Hyperion NIR bands in the selected biomass prediction

Table 4

Best Hyperion wavebands for predicting rainforest vegetation dry weight biomass determined based on lambda vs. lambda plots of the two-band vegetation indices (TBVIs)

Waveband number	Waveband center (nm)	Rank <sup>a</sup>	Remarks
<i>Ultraviolet (UV)</i>			
15	499	13	End of blue band. Sensitive to senescing, carotenoid, browning, and soil background effects (Thenkabail et al., 1999, 2000a).
<i>Visible</i>			
26	611	14	Absorption portion. Sensitive to biomass and LAI. Similar to 682 nm.
33	682	1	Absorption maxima 1. Sensitive to biomass and LAI. Greatest soil-crop contrast in 350–2500 nm (Thenkabail et al., 2000a, 2002).
34	692	10	Absorption maxima 2. Start of rapid change of slope leading to red-edge (700–740 nm). Sensitive to vegetation biomass and LAI.
<i>Red-edge</i>			
37	722	11	Center of red-edge. Sensitive to vegetation stress and dynamics (Dawson & Curran, 1998; Elvidge & Chen, 1995).
<i>Near-infrared (NIR)</i>			
43	783	7	Early NIR. More sensitive to changes in chlorophyll content than a broad NIR band (Curran et al., 1992).
49	845	21	Center of “NIR shoulder”. Strong correlation with total chlorophyll (Schepers et al., 1996).
54	895	8	NIR peak. Sensitive to total chlorophyll, biomass, LAI, and protein (Thenkabail et al., 2000a, 2002).
<i>Moisture sensitive NIR (MSNIR)</i>			
79, 80	943	22	Moisture absorption trough maxima. Sensitive to plant moisture status.
91	1054	15	Reflective peak soon after moisture absorption trough in NIR. Sensitive to plant moisture status.
95	1094	16	Post reflectance peak in NIR. Sensitive to biomass and LAI.
<i>Far near infrared (FNIR)</i>			
95–96	1104	6	FNIR rapidly raising spectra. A point of most rapid rise in spectra with change in wavelength in FNIR. Sensitive to biomass and LAI.
100	1145	17	FNIR absorption area. A small region of minor absorption area. Sensitive to plant moisture and biomass.
107	1215	5	FNIR rapidly falling spectra. A point of most rapid change fall in spectra with change in wavelength in FNIR. Sensitive to plant moisture.
114	1286	12	Reflectance peak in FNIR. Sensitive to biomass and LAI.

Table 4 (continued)

Waveband number	Waveband center (nm)	Rank <sup>a</sup>	Remarks
<i>Early mid-infrared (EMIR)</i>			
132	1467	3	EMIR minor peak. Sensitive to changes in plant moisture.
137–138	1518	23	EMIR rapidly raising spectra. A point of rapid increase in spectra per unit change in wavelength in EMIR. More sensitive to changes in plant moisture content than in NIR (Jensen, 2000).
151	1659	9	EMIR reflectance pre-peak/peak in EMIR. Sensitive to lignin, biomass, starch. Most useful to discriminate different kinds of leaves (Gausman, 1973).
156	1710	2	EMIR rapidly falling spectra. A point of rapid fall in spectra per unit change in wavelength in EMIR. Sensitive to changes in canopy moisture content (Jensen, 2000).
<i>Far mid-infrared (FMIR)</i>			
187	2022	18	FMIR rapidly raising spectra. Sensitive to plant moisture.
190	2052	4	FMIR Moisture absorption trough 1. Sensitive to proteins (Kumar et al., in press).
211	2264	19	FMIR rapidly falling spectra. A point of most rapid change in slope of spectra based on land cover, vegetation type, and vigor. Sensitive to changes in plant moisture content (Jensen, 2000).
216	2315	20	FMIR moisture absorption trough 2. Area of minor trough in FMIR. Sensitive to plant moisture, stress, lignin, and starch.

<sup>a</sup> Ranking is based on the frequency of occurrence of wavebands in TBVI models.

models were centered at 783 nm (Hyperion band 43) and 895 nm (Hyperion band 54). The narrow waveband centered at 783 nm is known to be more sensitive to changes in chlorophyll content than broader NIR bands (Curran et al., 1992). The band centered around 895 nm captured the peak reflectance region for most vegetation, reaffirming previous studies indicating the importance of this waveband (e.g., Thenkabail et al., 2000a, 2002). The reflectance centered at 970 or 980 nm to that of reference wavelength 895 or 900 nm is known to be sensitive to leaf water content (Penuelas et al., 1993; Thenkabail, 2002). The waveband centered at 1659 nm (Hyperion band 151) is useful in discriminating among leaf types (Gausman, 1973) much like the waveband centered at 680 nm. The waveband centered at 692 nm (Hyperion band 34) carries similar information to Hyperion band 35, but can be more sensitive to certain vegetation growth stages or conditions. The 722-nm waveband (Hyperion band 37) is at the center of the red-edge for rainforest vegetation, and also coincides with the red-edge for agricultural crops.

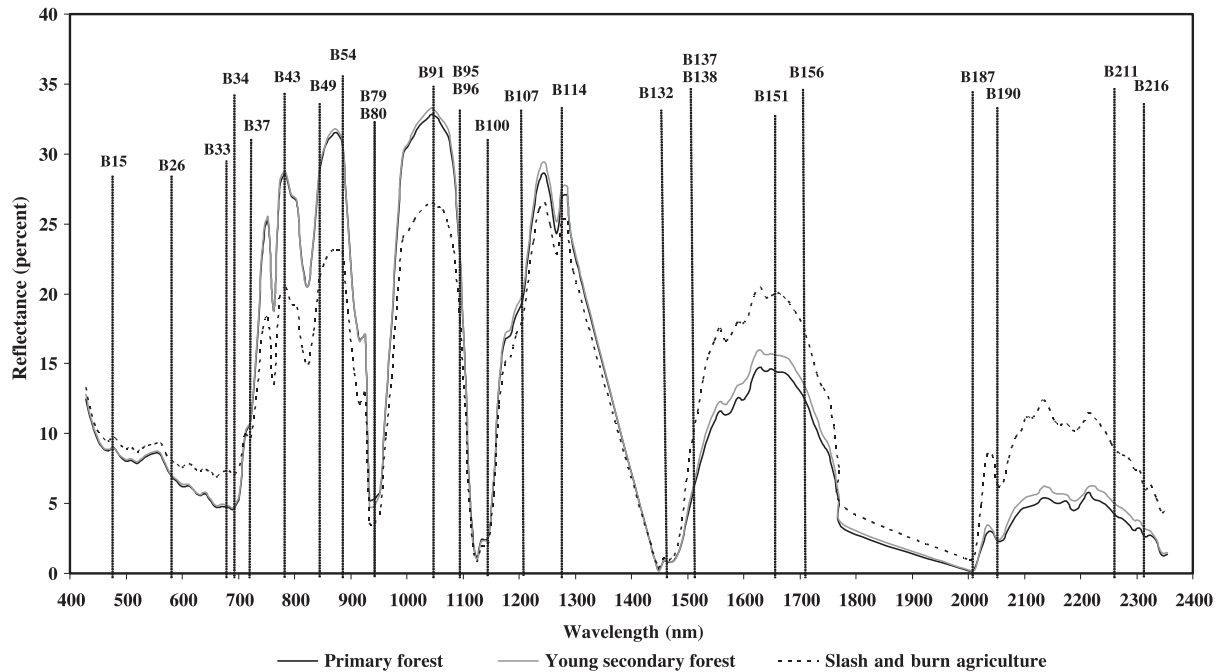


Fig. 8. Optimal Hyperion wavebands for predicting rainforest dry weight biomass (see Table 4).

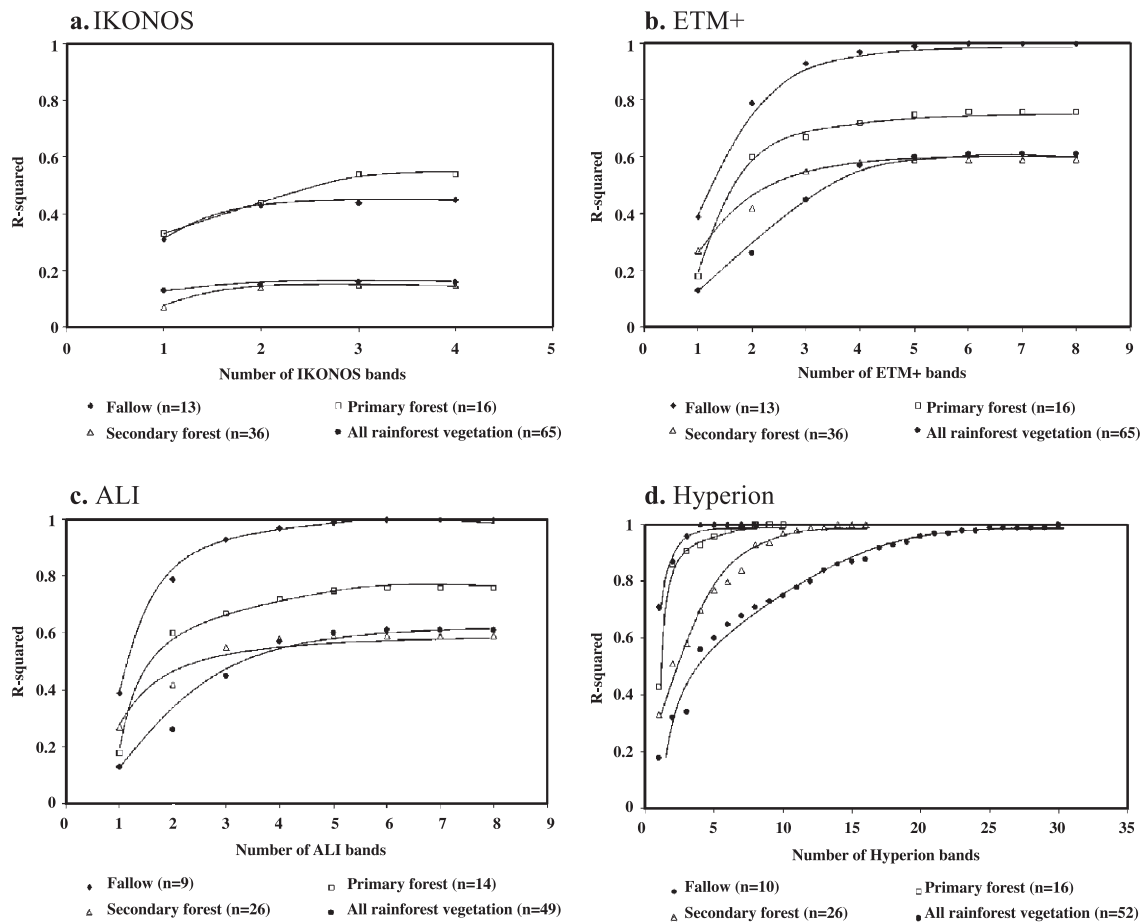


Fig. 9. Coefficients of determination ( $R^2$ ) for dry weight biomass prediction models based on optimal multiple band vegetation indices for the (a) IKONOS, (b) ETM+, (c) ALI, and (d) Hyperion sensors.



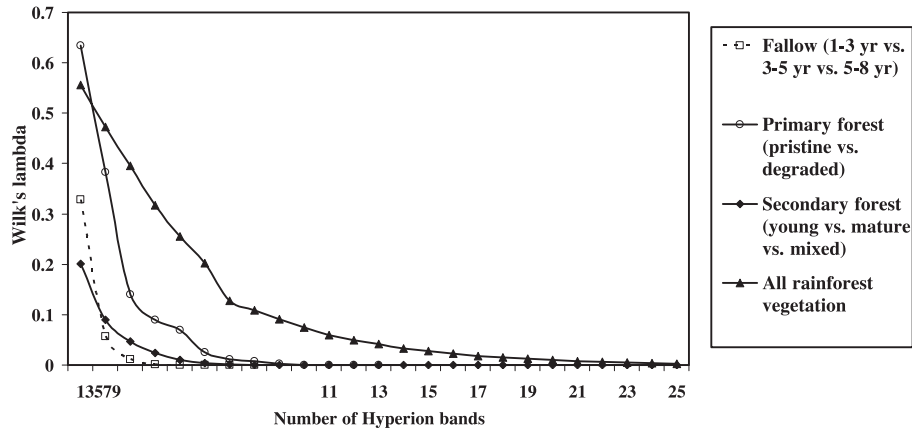


Fig. 10. Degree of separability for various groups of rainforest vegetation using Wilk's Lambda.

#### 5.4. Comparison of Hyperion results with broadband sensors

The 1-variable to  $n$ -variable OMBHVI models were developed for each sensor and for primary forest, secondary forest, fallow, and all rainforest vegetation combined. As expected, there was a rapid increase in the  $R^2$  values as the first few bands were added to the models for each sensor, but the rate of increase declined steadily thereafter (Fig. 9). For all rainforest vegetation combined, the  $R^2$  values for IKONOS and ETM+ were only 0.16 and 0.13, respectively, and there was little or no increase in the  $R^2$  beyond two or three bands. For ALI, an  $R^2$  value of 0.60 was reached when five bands were considered. On the other hand, dramatic increases in  $R^2$  values were possible when Hyperion narrowbands were considered (Fig. 9d). When five Hyperion narrowbands were

used the  $R^2$  value was 0.65, steadily increasing to reach an  $R^2$  value of 0.96 when 20 Hyperion bands were used. Overall, the Hyperion narrowbands explained 36–83% more of the variability in biomass among plots than the broadband sensors (Fig. 9). For primary forests and secondary forests, the broadband IKONOS and ETM+ sensors performed poorly (Fig. 9a and b). The  $R^2$  values for the ALI sensor were 0.75 for primary forest and 0.59 for secondary forest. Hyperion reached a  $R^2$  value of 0.98 for both primary and secondary forests when 6–11 bands were used. For fallows, Hyperion reached a perfect  $R^2$  value of one with four bands while ALI reached the same value with seven bands. Performances of the ETM+ and IKONOS sensors were substantially lower for the fallows.

The results highlight the distinct value of the Hyperion sensor's additional narrowbands when compared to the

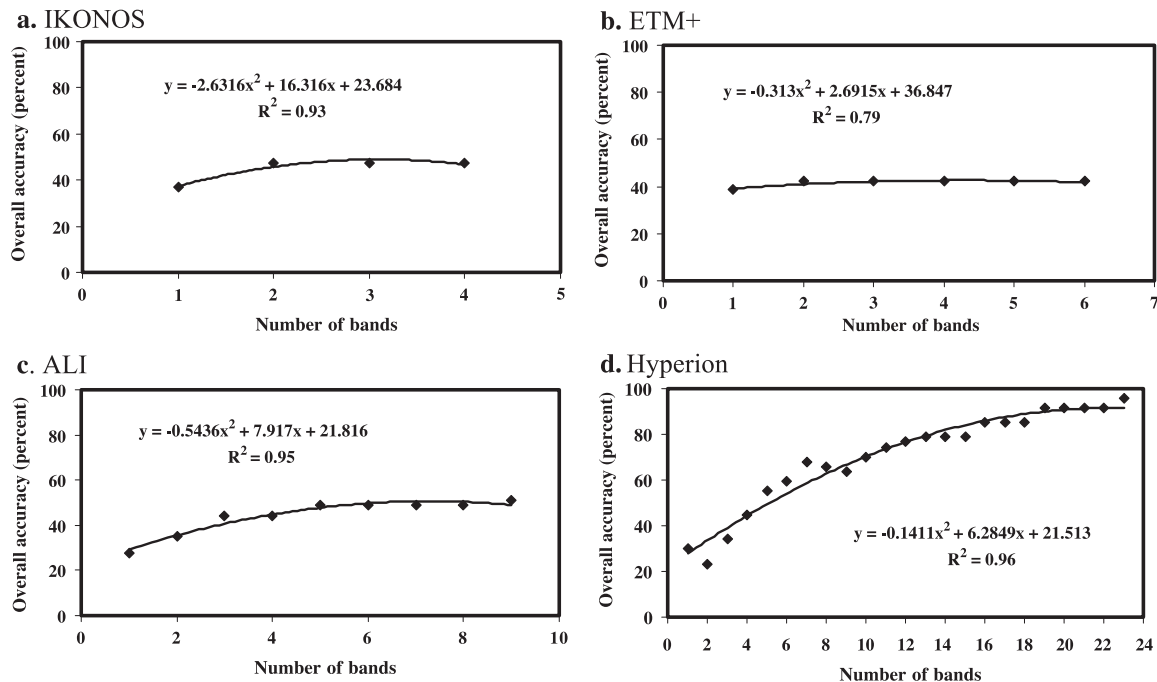


Fig. 11. Overall accuracies for rainforest LULC classification vs. number of bands used for the (a) IKONOS, (b) ETM+, (c) ALI, and (d) Hyperion sensors.

broadband sensors. Of the broadband sensors, ALI performed significantly better than ETM+ or IKONOS. This is likely the result of a combination of three factors: (a) additional wavebands; (b) better signal to noise ratios; and (c) radiometry. The ALI sensor has nine bands (Table 1) compared to six non-thermal ETM+ bands and four IKONOS bands. The signal to noise ratio of the ALI sensor is known to be five times better than that for the ETM+ sensor (NASA, 2002). The 16-bit ALI data also provides greater dynamic ranges for capturing subtle changes in landscape compared to the 8–11 bit ETM+ and IKONOS data.

The broadband sensors failed to explain a large proportion of the variability in biomass (Fig. 9). This was a result of: (a) broad band widths (relative to Hyperion); and (b) fewer wavebands. Indices derived from narrowbands are also known to provide greater sensitivity to subtle changes, reducing the sensor saturation problems of broadbands. Sensor saturation was a problem with the older generation of sensors (see Curran et al., 1997; Foody et al., 1996; Moran et al., 1994; Sader et al., 1994; Thenkabail, 1999; Steininger, 1996) and is still present in the new generation broadband IKONOS and ETM+ sensors, and to a lesser

extent in the ALI sensor. The Hyperion sensor, with many narrowbands spanning specific spectral ranges, is less prone to saturation when imaging rainforest vegetation.

### 5.5. Derivative greenness Hyperion vegetation index (DGHVI) models

Of the 10 DGHVIs examined, the only significant predictive model ( $R^2=0.83$ ) was for fallow biomass using DGV19 (428–906 nm). Otherwise, TBHVIs were more strongly correlated with biomass estimates. Therefore, DGHVIs were not considered further.

### 5.6. Discrimination or separability analysis

The ability of Hyperion data to spectrally separate different classes of rainforest vegetation was examined using stepwise discriminant analysis (SDA) and Wilks' Lambda (Fig. 10). Lower values of Wilk's Lambda correspond to greater separability, and vice versa. Wilk's Lambda approached zero (perfect separability) using 7–23 Hyperion bands when separating different classes of rainforest vege-

Table 5

Discriminant model confusion matrix of rainforest LULC vegetation classes using 23 Hyperion narrowbands

Generalized squared distance function :  $D_j^2(X) = (X - \bar{X}_j) \text{COV}^{-1} (X - \bar{X}_j)$

Posterior probability of membership in each LULC :  $Pr(j | X) = \exp(-0.5D_j^2(X)) / \sum_k \exp(-0.5D_k^2(X))$

Number (percent) of plots classified into LULC classes										
LULC	Fallow (1–3 years)	Fallow (3–5 years)	Fallow (5–8 years)	Primary forest	Disturbed primary forest	Mature secondary forest	Mixed secondary forest	Young secondary forest	Total	Errors of commission (%)
Fallow (1–3 years)	5 (100.0)	0 (0.0)	0 (0.0)	0 (0.0)	0 (0.0)	0 (0.0)	0 (0.0)	0 (0.0)	5 (100.0)	0
Fallow (3–5 years)	0 (0.0)	3 (100.0)	0 (0.0)	0 (0.0)	0 (0.0)	0 (0.0)	0 (0.0)	0 (0.0)	3 (100.0)	0
Fallow (5–8 years)	0 (0.0)	0 (0.0)	2 (100.0)	0 (0.0)	0 (0.0)	0 (0.0)	0 (0.0)	0 (0.0)	2 (100.0)	0
Primary forest	0 (0.0)	0 (0.0)	0 (0.0)	12 (92.3)	0 (0.0)	0 (0.0)	0 (0.0)	1 (7.7)	13 (100.0)	8
Disturbed primary forest	0 (0.0)	0 (0.0)	0 (0.0)	0 (0.0)	3 (100.0)	0 (0.0)	0 (0.0)	0 (0.0)	3 (100.0)	0
Mature secondary forest	0 (0.0)	0 (0.0)	0 (0.0)	0 (0.0)	0 (0.0)	6 (100.0)	0 (0.0)	0 (0.0)	6 (100.0)	0
Mixed secondary forest	0 (0.0)	0 (0.0)	0 (0.0)	0 (0.0)	0 (0.0)	0 (0.0)	12 (100.0)	0 (0.0)	12 (100.0)	0
Young secondary forest	0 (0.0)	0 (0.0)	0 (0.0)	0 (0.0)	0 (0.0)	0 (0.0)	1 (12.5)	7 (87.5)	8 (100.0)	12
Total	5 (9.6)	3 (5.8)	2 (3.9)	12 (23.1)	3 (5.8)	6 (11.5)	13 (25.0)	8 (15.4)	52 (100.0)	
Errors of omission (%)	0	0	0	0	0	0	8	12	overall accuracy = 96.1%	

$$K_{\text{hat}} = \left[ N \sum_{i=1}^r X_{ii} - \sum_{i=1}^r X_{+i}(X_{i+}) \right] / \left[ N^2 \sum_{i=1}^r X_{i+}(X_{+i}) \right]$$

where  $r$  is the number of rows in the matrix,  $X_{ii}$  is the number of observations in row  $i$  and column  $i$ ,  $X_{i+}$  and  $X_{+i}$  are the marginal totals of  $i$  and column  $i$ , respectively, and  $N$  is the total number of observations (Bishop et al., 1975).

Thereby,  $K_{\text{hat}} = [(52)(50) - 624] / [(52)^2 - 624] = 0.96$ ; where  $(5 \times 5) + (3 \times 3) + (2 \times 2) + (12 \times 13) + (3 \times 3) + (6 \times 6) + (13 \times 12) + (8 \times 8) = 624$ .

tation (Fig. 10). Only 7–9 Hyperion bands were required to separate pristine vs. degraded primary forest, young vs. mature vs. mixed secondary forest, and fallows of 1–3, 3–5, or 5–8 years. When all rainforest vegetation was pooled approximately 23 Hyperion bands were required to achieve adequate separability (Fig. 10).

## 6. Results and discussions—use of images to separate LULC classes

### 6.1. Overall accuracies of broadband and narrowband data using discriminant model

In order to determine the discriminatory power of narrowband Hyperion data relative to broadband IKONOS, ETM+, and ALI data, we classified the same nine forest LULC classes (Fig. 2) using data from various band combinations of each sensor. Overall accuracies (Fig. 11) for rainforest LULC classification vs. number of bands used for the (a) IKONOS, (b) ETM+, (c) ALI, and (d) Hyperion sensors. The same number of field plot data (see Section 2.2 and its subsections) was used in discriminant model. The resulting discriminant models were used to construct error matrices from classifications based on 1 to  $n$ th bands. A sample error matrix from a 23 Hyperion band discriminant model is given in Table 5. Overall accuracies were computed and are plotted against the number of bands used in Fig. 11. The results show that the highest overall accuracies for classifying nine forest LULC classes were 48% for IKONOS (all four bands), 42% for ETM+ (all six non-thermal bands), 51% for ALI (nine bands), and 96% for Hyperion (23 bands). However, the accuracies are only marginally lower for IKONOS and ETM+ with only two or three bands, and for ALI with only five bands. The results followed a similar pattern of the results obtained by distinctly different methods as described in Sections 5.2.3 and 5.3.

Classification accuracies were generally low (Fig. 11). This may be attributed to the complexity of the forest LULC classes considered (Fig. 2). Among the broadband sensors, the most sensitive classification results were obtained with ALI (Fig. 11c), closely followed by IKONOS (Fig. 11a) and ETM+ (Fig. 11b). The overall accuracies were between 45% and 52% higher with the Hyperion data.

## 7. Conclusions

The study established the advantages of using narrowband Hyperion data over broadband IKONOS, ETM+, and ALI data in studying rainforest vegetation. When compared to broadband data from IKONOS, ETM+, and ALI sensors, Hyperion narrowbands (1) explained 36–83% more of the variability in biomass and (2) increased LULC classification accuracies by 45–52%. The study also identified 23 most sensitive Hyperion bands (Table 4) for predicting rainforest

biomass; band widths were 10–20 nm. The overall accuracy in classifying nine rainforest LULC classes was 96% and was achieved using these 23 Hyperion wavebands. In comparison, the overall accuracies were only 48% for IKONOS (four bands), 42% for ETM+ (six non-thermal bands) and 51% for ALI (nine multispectral bands).

Overall, data mining techniques and biomass modeling highlighted the importance of MIR bands, specifically from the EMIR (1300–1900 nm) region. The study focused on the spectral characteristics of the sensors, but spatial resolution may also provide important information in the discrimination of biophysical characteristics if spatial or textural analyses are also included.

## Acknowledgements

This research was made possible through a generous grant from NASA (grant number: NAG5-9437). The project is funded under the Investigations that Contribute to the NASA Earth Science Enterprise's Modeling and Data Analysis (NRA-99-OES-04) program, which comes under the Pathfinder Data Set and Associated Science Program (PDSP). IKONOS data was provided by a data grant under NASA Scientific Data Purchase (SDP), funded under the Earth Science Enterprise (ESE) Program to provide scientific data to the ESE science community. We are very grateful for the enthusiastic field support provided by the International Institute of Tropical Agriculture (IITA), Humid Forest Station (HFS), of Cameroon. We specifically would like to thank Dr. Stephan Weise, Dr. Dyno Keatinge, and Ms. Valentina Robiglio of IITA for their co-operation and collaboration. Thanks also to Dr. Christian Nolte of IITA HFS for providing the fallow biomass measurements and help in describing the study area. Excellent field work was carried out in very difficult conditions by Mr. Engueng Michel and his team. We gratefully acknowledged this support. Mr. Salaou Amaou is thanked for driving. Finally, the anonymous reviewers helped us re-organize our presentation and provide focus and clarity in presentation. We greatly appreciate the comprehensive comments and suggestions made by the two reviewers.

## References

- Anderson, J. R., Hardy, E. E., & Roach, J. T. (1976). A land use and land cover classification system for use with remote sensor data. *A revision of the land use classification system as presented in U.S. Geological Survey Circular 671. Geological Survey Professional Paper, 964*, Washington: United States Government Printing Office.
- Bishop, Y., Fienberg, S., & Holland, P. (1975). *Discrete multivariate analysis: Theory and practice*. Cambridge, MA: MIT Press.
- Blackburn, G. A. (1999). Relationships between spectral reflectance and pigment concentrations in stacks of deciduous broadleaves. *Remote Sensing of Environment*, 70(2), 224–237.
- Blackburn, G. A., & Milton, E. J. (1995). Seasonal variations in the spectral reflectance of deciduous tree canopies. *International Journal of Remote Sensing*, 16(4), 709–720.

- Boyd, D. S., & Duane, W. J. (2001). Exploring spatial and temporal variation in middle infrared reflectance (at 3.75  $\mu\text{m}$ ) measured from the tropical forests of West Africa. *International Journal of Remote Sensing*, 22(10), 1861–1878.
- Brondizio, E., Moran, E., Mausel, P., & Wu, Y. (1996). Land cover in the Amazon estuary: Linking of the Thematic Mapper with botanical and historical data. *Photogrammetric Engineering and Remote Sensing*, 62, 921–929.
- Brown, S. (1997). *Estimating biomass and biomass change of tropical forests: A primer*. Rome, Italy: Food and Agriculture Organization of the United Nations.
- Carter, G. A. (1998). Reflectance bands and indices for remote estimation of photosynthesis and stomatal conductance in pine canopies. *Remote Sensing of Environment*, 63, 61–72.
- Chavez, P. S. (1986). An improved dark-object subtraction technique for atmospheric scattering correction of multispectral data. *Remote Sensing of Environment*, 24, 459–479.
- Chavez, P. S. (1996). Image-based atmospheric corrections—revisited and improved. *Photogrammetric Engineering and Remote Sensing*, 62(9), 1025–1036.
- Curran, P. J., Dungan, J. L., Macler, B. A., Plummer, S. E., & Peterson, D. L. (1992). Reflectance spectroscopy of fresh whole leaves for the estimation of chemical concentration. *Remote Sensing of Environment*, 39(2), 153–166.
- Curran, P. J., Foody, G. M., Lucas, R. M., Honzak, M., & Grace, J. (1997). The carbon balance of tropical forests: From the local to the regional scale. In P. R. van Gardingen, G. M. Foody, & P. J. Curran (Eds.), *Scaling-up from cell to landscape* (pp. 201–227). Cambridge: Cambridge Univ. Press.
- Dawson, T. P., & Curran, P. J. (1998). A new technique for interpolating the reflectance red edge position. *International Journal of Remote Sensing*, 19(11), 2133–2139.
- De Jong, B. H. J., Gaona, S. O., Santiago, M. A. C., Marcial, N. R., & Cairns, M. A. (2000). Carbon flux and patterns of land-use/land-cover change in the Selva Lacandona, Mexico. *Ambio*, 29(8), 504–511.
- Draper, N. R., & Smith, H. (1981). *Applied regression analysis*. New York: Wiley.
- Elvidge, C. D., & Chen, Z. (1995). Comparison of broad-band and narrow-band red and near-infrared vegetation indices. *Remote Sensing of Environment*, 54, 38–48.
- Foody, G. M., Palubinskas, G., Lucas, R. M., Curran, P. J., & Honzak, M. (1996). Identifying terrestrial carbon sinks: Classification of successional stages in regenerating tropical forest from Landsat TM data. *Remote Sensing of Environment*, 55, 205–216.
- Gausman, H. W. (1973). Reflectance, transmittance, and absorptance of light by subcellular particles of spinach (*Spinacia oleracea* L.) leaves. *Agronomy Journal*, 65, 551–553.
- Gross, H., & Scott, J. (1998). Application of spectral mixture analysis and image fusion techniques or images sharpening. *Remote Sensing of Environment*, 63, 85–94.
- Hauser, S., & Nolte, C. (2002). Biomass production and N fixation of five *Mucuna pruriens* varieties and their effect on maize yields in the forest zone of Cameroon. *Journal of Plant Nutrition and Soil Science*, 165(10), 101–109.
- Jakubauskas, M. E., & Price, K. P. (1997). Empirical relationships between biotic and spectral factors of Yellowstone lodgepole pine forests. *Photogrammetric Engineering and Remote Sensing*, 63(12), 1375–1381.
- Jensen, J. R. (2000). *Remote sensing of the environment: An earth resource perspective*. Upper Saddle River, NJ: Prentice-Hall.
- Klecka, W. R. (1980). Discriminant analysis. *Quantitative Applications in Social Sciences Series*, vol. 19. Thousand Oaks, CA: Sage Publications.
- Kumar, L., Schmidt, K. S., Dury, S., & Skidmore, A. K. (2001). Review of hyperspectral remote sensing and vegetation science. In F. van der Meer (Ed.), *Hyperspectral Remote Sensing*. Dordrecht: Kluwer Academic Publishing (In press).
- Lambert, N. J., Ardo, J., Rock, B. N., & Vogelmann, J. E. (1995). Spectral characterization and regression-based classification of forest damage in Norway spruce stands in the Czech Republic using Landsat Thematic Mapper data. *International Journal of Remote Sensing*, 16, 1261–1287.
- Lévesque, J., & King, D. J. (2003). Spatial analysis of radiometric fractions from high-resolution multispectral imagery for modelling individual tree crown and forest canopy structure and health. *Remote Sensing of Environment*, 84(4), 589–602.
- Markham, B. L., & Barker, J. L. (1985). Spectral characterization of the LANDSAT Thematic Mapper sensors. *International Journal of Remote Sensing*, 6(5), 697–716.
- Markham, B. L., & Barker, J. L. (1987). Radiometric properties of U.S. processed Landsat MSS data. *Remote Sensing of Environment*, 22, 39–71.
- Moran, E. F., Brondizio, E., Mausel, P., & Wu, Y. (1994). Integrating Amazonian vegetation, land-use, and satellite data. *Bioscience*, 44, 329–338.
- National Aeronautics and Space Administration (NASA) (2002). Earth observing—1: Advanced land imager. (<http://eo1.gsfc.nasa.gov/Technology/ALHome1.htm>).
- Neckel, H., & Labs, D. (1984). The solar radiation between 3300 and 12500 Å. *Solar Physics*, 90, 205–258.
- Nolte, C., & Hauser, S. (2002). Natural fallows in the humid zone of West and Central Africa: Their biomass production, nutrient accumulation and nutrient budget. *Agriculture, Ecosystems and Environment* (in review).
- Olson, C. E. (1967). Optical remote sensing of the moisture content in fine forest fuels. *1st Report N8036-1-F*. Ann Arbor, MI: University of Michigan.
- Penuelas, J., Filella, I., Biel, C., Serrano, L., & Save, R. (1993). The reflectance at the 950–970 region as an indicator of plant water status. *International Journal of Remote Sensing*, 14(10), 1887–1905.
- Rao, C. R. (1973). *Linear statistical inference and its applications*. New York: Wiley.
- Sader, S. A., Sever, T., Smoot, J. C., & Richards, M. (1994). Forest change estimates for the northern Peten region of Guatemala—1986 to 1990. *Human Ecology*, 22(3), 317–332.
- Salas, W. A., Ducey, M. J., Rignot, E., & Skole, D. (2002). Assessment of JERS-1 SAR for monitoring secondary vegetation in Amazonia: I. Spatial and temporal variability in backscatter across a chrono-sequence of secondary vegetation stands in Rondonia. *International Journal of Remote Sensing*, 23(7), 1357–1379.
- Sampson, P. H., Treitz, P. M., & Mohammed, G. H. (2001). Remote sensing of forest condition in tolerant hardwoods: An examination of spatial scale, structure and function. *Canadian Journal of Remote Sensing*, 27(3), 232–246.
- SAS Institute (1999). *SAS/STAT user's guide and software release, version 6.12 Ed.* Cary, NC: SAS Institute.
- Schepers, J. S., Blackmer, T. M., Wilhelm, W. W., & Resende, M. (1996). Transmittance and reflectance measurements of corn leaves from plants with different nitrogen and water supply. *Journal of Plant Physiology*, 148, 523–529.
- Space Imaging (2001). *IKONOS relative spectral response and radiometric calibration coefficients, document no. SE-REF-016*, Rev. A. Thorton, CO: Space Imaging.
- Steininger, M. K. (1996). Tropical secondary forest regrowth in the Amazon: Age, area and change estimation with Thematic Mapper data. *International Journal of Remote Sensing*, 17, 9–27.
- Steininger, M. K. (2000). Satellite estimation of tropical secondary forest above-ground biomass: Data from Brazil and Bolivia. *International Journal of Remote Sensing*, 21(6), 1139–1157.
- Thenkabail, P. S. (1999). Characterisation of the alternative to slash-and-burn benchmark research area representing the Congolese rainforests of Africa using near-real-time SPOT HRV data. *International Journal of Remote Sensing*, 20(5), 839–877.
- Thenkabail, P. S. (2002). Optimal hyperspectral narrowbands for discriminating agricultural crops. *Remote Sensing Reviews*, 20, 257–291.
- Thenkabail, P. S., Hall, J., Lin, T., Ashton, M. S., Harris, D., & Enclona, E. A. (2003). Detecting floristic structure and pattern across topogra-



- phic and moisture gradients in a mixed species Central African forest using IKONOS and Landsat-7 ETM+ images. *International Journal of Applied Earth Observation and Geoinformation*, 4, 255–270.
- Thenkabail, P. S., Nolte, C., & Lyon, J. G. (2000b). Remote sensing and GIS modeling for selection of benchmark research area in the inland valley agroecosystems of West and Central Africa. *Photogrammetric Engineering and Remote Sensing, Africa Applications Special Issue*, 66 (6), 755–768.
- Thenkabail, P. S., Smith, R. B., & De Pauw, E. (1999). Hyperspectral vegetation indices for determining agricultural crop characteristics. *CEO Research Publication Series, vol. 1*. New Haven, CT, USA: Center for Earth Observation, Yale University.
- Thenkabail, P. S., Smith, R. B., & De Pauw, E. (2000a). Hyperspectral vegetation indices and their relationships with agricultural crop characteristics. *Remote Sensing of Environment*, 71, 158–182.
- Thenkabail, P. S., Smith, R. B., & De Pauw, E. (2002). Evaluation of narrowband and broadband vegetation indices for determining optimal hyperspectral wavebands for agricultural crop characterization. *Photogrammetric Engineering and Remote Sensing*, 68(6), 607–621.
- Thenkabail, S. P., Ward, A. D., Lyon, J. G., & Merry, C. J. (1994). Thematic Mapper vegetation indices for determining soybean and corn crop growth parameters. *Photogrammetric Engineering and Remote Sensing*, 60(4), 437–442.
- Townend, J. (2002). *Practical statistics for environmental and biological scientists*. West Sussex, England: Wiley.
- Walter, H. (1985). *Vegetation of the earth and ecological systems of the geo-biosphere*. (3rd ed.). New York: Springer-Verlag.
- Whitmore, T. C. (1998). *An introduction to tropical rainforests*. Oxford: Oxford Univ. Press.